C. R. Mecanique 343 (2015) 518–532

Contents lists available at ScienceDirect

Comptes Rendus Mecanique

www.sciencedirect.com

Discrete simulation of fluid dynamics

Local boundary reflections in lattice Boltzmann schemes: Spurious boundary layers and their impact on the velocity, diffusion and dispersion

Irina Ginzburg *, Laetitia Roux, Goncalo Silva

IRSTEA, Antony Regional Centre, HBAN, 1, rue Pierre-Gilles-de-Gennes, CS 10030, 92761 Antony cedex, France

ARTICLE INFO

Article history:
Received 25 November 2014
Accepted 22 March 2015
Available online 20 August 2015

Keywords:
Normal flux boundary condition
Advection–diffusion lattice Boltzmann schemes
Boundary layer
Tangential flux
Pure diffusion
Taylor dispersion
Boundary-layer dispersion
Equilibrium weights
Two-relaxation-time LBM scheme
Recurrence equations
Exact solutions of numerical scheme

ABSTRACT

This work demonstrates that in advection–diffusion Lattice Boltzmann schemes, the local mass-conserving boundary rules, such as bounce-back and local specular reflection, may modify the transport coefficients predicted by the Chapman–Enskog expansion when they enforce to zero not only the normal, but also the tangential boundary flux. In order to accommodate it to the bulk solution, the system develops a Knudsen-layer correction to the non-equilibrium part of the population solution. Two principal secondary effects—(i) decrease in the diffusion coefficient, and (ii) retardation of the average advection velocity, obtained in a closed analytical form, are proportional, respectively, to freely assigned diagonal weights for equilibrium mass and velocity terms. In addition, due to their transverse velocity gradients, the boundary layers affect the longitudinal diffusion coefficient similarly to Taylor dispersion, as they grow as the square of the Péclet number. These numerical artifacts can be eliminated or reduced by a proper space distribution of the free-tunable collision eigenvalue in two-relaxation-time schemes.

1. Introduction

In this work, we examine the modification of the bulk equilibrium by the local mass-conserving boundary conditions in the framework of the Lattice Boltzmann Method (LBM). The Knudsen boundary layers are usually considered in the context of the rarefied gas dynamics as boundary conditions for non-equilibrium flows [1]. A very comprehensive critical review on the efforts devoted to appropriate LBM boundary conditions can be found in works [2,3]. The objective of this work is quite different. We consider the two-dimensional LBM for linear advection–diffusion in the Poiseuille profile $U_x(y)$ in a straight channel of width H bounded by impermeable walls (Figs. 1 and 2a). The pioneering advection–dispersion models [4–6] apply the same equilibrium as the Navier–Stokes models, but they relax momentum conservation. As yet, the Neumann boundary conditions for zero concentration flux on the impermeable wall adopt the Maxwell population reflections. According to [7,8] the transverse velocity gradient induces a longitudinal dispersion of a passive scalar. While the non-local, specular-forward reflection matches the Taylor dispersivity properly, the local bounce-back (BB-rule) fails to do so [9]. However, the specular-forward reflection becomes inconvenient for curved boundaries.

* Corresponding author.
E-mail addresses: irina.ginzburg@irstea.fr (I. Ginzburg), roux.laetitia.th@gmail.com (L. Roux), goncalo.silva@irstea.fr (G. Silva).

http://dx.doi.org/10.1016/j.crme.2015.03.004
1631-0721/

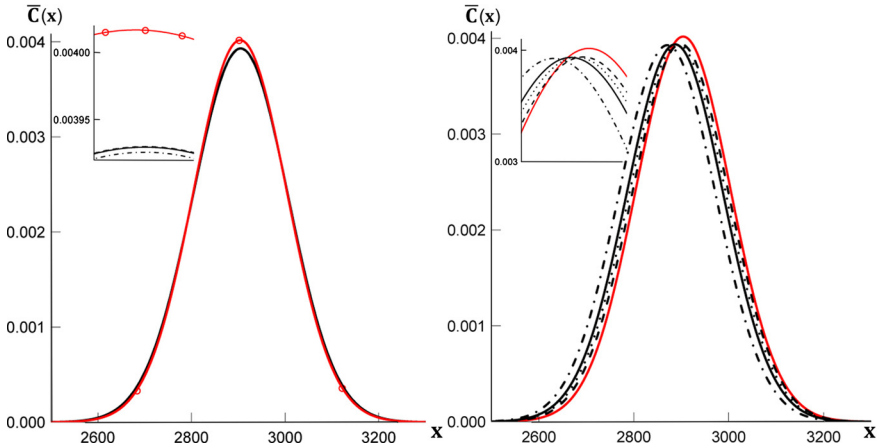

Fig. 1. (Color online.) The averaged concentration profiles in Poiseuille profile are computed with the "standard" hydrodynamic d2Q9 equilibrium applying the specular reflection (d2Q9-SNL, left) and bounce-back (d2Q9-BB, right) in a channel of width $H = 12$. The free product of two eigenfunctions in two-relaxation-time (TRT) collision is $\Lambda = \{\frac{1}{12}, \frac{1}{6}, \frac{1}{4}, \frac{1}{2}\}$ (dashed, dotted, solid, dash-dotted). The analytical solution with molecular diffusion $D_0 = \frac{1}{2}$ and averaged velocity $\mathcal{U} = \frac{2}{9}\sqrt{3}$ is plotted as the solid (red) line. (For interpretation of references to color in this figure caption, the reader is referred to the online version of this article.)

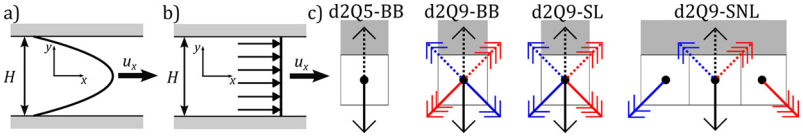

Fig. 2. (Color online.) Parabolic profile (p-field) and constant-velocity plug flow (c-field) are imposed in the channel. Two local: d2Q5-BB/d2Q9-BB and d2Q9-SL, and one non-local: d2Q9-SNL boundary reflections are applied for zero-normal-flux.

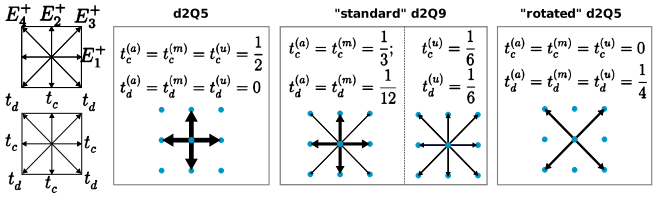

Fig. 3. (Color online.) Equilibrium d2Q9 weights are exemplified for (i) d2Q5, (ii) "standard" d2Q9 and (iii) "rotated" d2Q5.

Further analysis [10] shows that the bounce-back rule reduces the tangential boundary flux to zero via the diagonal (non-perpendicular with the wall) links. An example of concentration profiles is illustrated in Fig. 1 for those two boundary rules depicted in Fig. 2. It is displayed in Fig. 1 that in the framework of two-relaxation-time (TRT) advection–diffusion d2Q9-BB scheme [11,12], the bounce-back retardation of the profile depends on the free-tunable product Λ of two eigenfunctions Λ^- and Λ^+. Notice that, while in the fluid dynamics schemes [13,14] Λ^+ determines the kinematic viscosity and Λ^- is a free parameter, in ADE schemes they exchange their roles, that is $D_0 \propto \Lambda^-$ and Λ^+ is a free parameter. Our analysis will show that the amplitude of the bounce-back velocity correction scales proportionally to the free-tunable diagonal equilibrium velocity weight. It should be said that, while in the Navier–Stokes equilibrium the coordinate/diagonal velocity weights are fixed by two isotropic constraints [15], the ADE imposes only one constraint (Fig. 3). In particular, assigning a zero value to all diagonal weights, the d2Q9 reduces to the coordinate-stencil d2Q5 model, where the local and non-local specular reflections both reduce to the BB-rule (d2Q5-BB in Fig. 2) and the tangential defect on the straight walls vanishes.

Recall that the hydrodynamic schemes locate exactly the Poiseuille profile in straight or rotated channels, or in circular pipe, only when the boundary scheme accounts for the flow curvature in the non-equilibrium [16,17,13,14]. The Dirichlet boundary conditions of similar accuracy have been constructed for concentration in ADE [10] and pressure in NSE [13,14]. However, in practice, the mass-conserving Neumann boundary conditions are mostly needed in ADE, while the proposed conditions either do not necessarily conserve the mass for curved shapes, e.g., [10,18], or neglect the tangential flux variation and exclude the most interesting relaxation-parameter choice [19]. Therefore, the versatile, local and mass-conserving BB-rule is still appealing, especially for dispersion in porous media, and one of our objectives is to release its tangential constraint.

For this purpose, we firstly identify the underlying non-equilibrium mechanism following [20]. It exhibits the boundary layers that accommodate the bounce-back closure relation along each individual lattice direction. Similarly to Knudsen's boundary layers, their amplitude exponentially decays with the distance from the boundary. The coupling of the equilib-

rium and Chapman–Enskog bulk non-equilibrium with boundary layers occurs in grid boundary nodes via an individual closure relation of the boundary scheme. To the best of our knowledge, the exact construction of the non-equilibrium boundary layers has been undertaken only in a few works on LGA/LBM. In seminal work [21], the Kramers problem [1] is solved exactly in linear shear flow on the FHP discrete-velocity set, for parallel and perpendicular orientations of the wall. Remarkably, the Knudsen boundary-layer solution of the system depends on the shear rate and free-energy-flux collision rates, in the form identified later as a free product Λ of two eigenfunctions in TRT schemes. The work [21] concludes that the (probabilistic) p-combination of the bounce-back and specular reflection does not support the layers, but results in an anisotropic, p-dependent location of the no-slip tangential velocity. The alternative analysis technique [22,23] adopts the Chapman–Enskog and Taylor expansions to show that the specific anisotropic p-dependent Λ values enable the exact location of the no-slip bounce-back walls in parallel/diagonal Poiseuille flow; the same solutions remain valid for different velocity sets [17,13,14,24]. On the other hand, the non-equilibrium boundary layers [14] explain why both Stokes and Navier–Stokes equilibrium distributions produce the same effective parabolic profile, although their respective second- and fourth-order Chapman–Enskog solutions obey quite different closure conditions. This analysis was also applied to different second- and third-order accurate hydrodynamic boundary schemes [14]. The analysis developed in works [16,25] shows that in stair-wise discretized rotated channels the ensemble of the discrete bounce-back closure relations is deficient because of their intrinsic local mass conservation, while the mass is only conserved over the period of the cell on the exact population solution of the problem. Because of this discrepancy, the modeled parabolic profile is superposed on the boundary-layer velocity profile, meaning that the non-equilibrium boundary layer is projected on the discrete velocity vectors, thus modifying the prediction of the Chapman–Enskog analysis [16].

The distinctive point of our analysis for the ADE is that we show that the accommodation layers may directly modify the transport coefficients consistently derived with the help of the Chapman–Enskog analysis. Taking as example both plug and Poiseuille flows, c-field and p-field hereafter, we establish that the bounce-back and local specular reflection modify (i) the effective diffusion coefficient proportionally to the free-tunable diagonal mass-weight value, and (ii) the effective advection velocity proportionally to the free-tunable diagonal velocity weight. The diffusion effect is velocity independent and it manifests itself even in pure diffusion. The velocity effect results in the longitudinal Taylor numerical dispersion due to the transverse velocity gradients inside the boundary layer. The specular-forward reflection does not produce any boundary effects and the difference between the measured apparent dispersion and the Taylor prediction happens only because of the truncation dispersion; its closed-form expression is derived in our parallel work [26] and reported here for the sake of completeness. With the bounce-back and local specular reflection, the three dispersions, namely, mechanical, truncation and boundary are combined together, enabling a formal improvement of the truncation error, but at the price of slowing down the advection front. Since the amplitudes of the boundary layers decrease as $\sqrt{\Lambda}$, we show that their effect can be eliminated or reduced by an appropriate choice of Λ in the boundary nodes.

The rest of the paper is organized as follows. Section 2 provides the necessary LBM basis and numerical observations of the bounce-back/local specular reflection effects in plug and Poiseuille profiles. Section 3 extends the non-equilibrium boundary-layer solutions [20]. Section 4 derives from these solutions the exact expressions for the averaged diffusion and advection corrections due to the bounce-back, then builds the corresponding dispersion. All these theoretical results are validated against the numerical measurements of the two first moments. Section 5 provides solution strategies for boundary layers reduction. Section 6 concludes this work.

2. Basis equations and numerical observations

The discrete, d-dimensional velocity set consists of zero vector $\mathbf{c}_0$ and $Q_m = Q - 1$ vectors $\mathbf{c}_q$ connecting square-grid nodes $\mathbf{r}$: each vector $\mathbf{c}_q$ has the opposite one, $\mathbf{c}_{\bar{q}} = -\mathbf{c}_q$. The corresponding populations $\{f_q(\mathbf{r},t)\}$ are decomposed into their symmetric and anti-symmetric components: $f_q^{\pm} = (f_q \pm f_{\bar{q}})/2$. The TRT scheme [10,13] updates them with the help of the two relaxation parameters $s^{\pm} \in]0,2[$:

$$f_q(\mathbf{r}+\mathbf{c}_q,t+1) = f_q(\mathbf{r},t) + g_q^+ + g_q^-\ ,\ q=0,\dots,\frac{Q_m}{2}\ ,\ g_0^+ = -2\sum_{q=1}^{Q_m/2} g_q^+\ ,\ g_0^- = 0\,,$$

$$f_{\bar{q}}(\mathbf{r}-\mathbf{c}_q,t+1) = f_{\bar{q}}(\mathbf{r},t) + g_q^+ - g_q^-\ ,\ q=1,\dots,\frac{Q_m}{2}\ ,\ g_q^{\pm} = -s^{\pm}(f_q^{\pm} - e_q^{\pm})\ ,\ q=1,\dots,\frac{Q_m}{2}\,. \tag{1}$$

The positive eigenfunctions $\Lambda^{\pm} = \frac{1}{s^{\pm}} - \frac{1}{2}$ determine the transport coefficients. A special role is played by their free-tunable product $\Lambda = \Lambda^-\Lambda^+$. Its particular values, such as $\Lambda = \frac{1}{12}$ and $\Lambda = \frac{1}{6}$, provide the third-/fourth-order accuracy at the steady state for any equilibrium, while $\Lambda = \frac{1}{4}$ has advanced stability in the ADE [11,12]. We consider the modelling of the two-dimensional advection–diffusion equation in the prescribed velocity field $\mathbf{U}(\mathbf{r})$ with the d2Q9 scheme. Let its four first velocities have components $c_x = \{1,0,1,-1\}$ and $c_y = \{0,1,1,1\}$ (see Fig. 3). The equilibrium distribution $e_q^{\pm}(\mathbf{r},t) = E_q^{\pm}(\mathbf{r})C(\mathbf{r},t)$ is set proportional to solute concentration $C(\mathbf{r},t) = f_0 + 2\sum_{q=1}^{Q_m/2} f_q^+$, and the set $\{E_q^{\pm}\}$ reads for $q = 1,\dots,Q_m/2$:

$$E_1^+ = t_c^{(m)} c_e + t_c^{(u)} \bar{U}^2 + \frac{(U_x^2 - U_y^2)}{4}\ ,\ E_2^+ = t_c^{(m)} c_e + t_c^{(u)} \bar{U}^2 - \frac{(U_x^2 - U_y^2)}{4}\ ,$$
$$E_3^+ = t_d^{(m)} c_e + t_d^{(u)} \bar{U}^2 + \frac{U_x U_y}{4}\ ,\qquad E_4^+ = t_d^{(m)} c_e + t_d^{(u)} \bar{U}^2 - \frac{U_x U_y}{4}\ ,\ \bar{U}^2 = \frac{1}{2}(U_x^2 + U_y^2)\ ,$$
$$E_1^- = t_c^{(a)} U_x\ ,\ E_2^- = t_c^{(a)} U_y\ ,\ E_3^- = t_d^{(a)}(U_x + U_y)\ ,\ E_4^- = -t_d^{(a)}(U_x - U_y)\ . \tag{2}$$

The weights obey one isotropic constraint: $2\sum_{q=1}^{Q_m/2} t_q^{(\cdot)} c_{q\alpha} c_{q\beta} = \delta_{\alpha\beta}$; the coordinates weights $t_c^{(\cdot)}$ can be selected independently for each of three families; the diagonal weights $t_d^{(\cdot)}$ are computed from them: $t_d^{(\cdot)} = 1/4 - t_c^{(\cdot)}/2$. Two "limit" distributions, such as the d2Q5 and "rotated" d2Q5, are specified in Fig. 3 along with the "standard" weights borrowed from the hydrodynamic scheme. The maximum velocity amplitude should obey weight-dependent stability conditions $|\mathbf{U}| \le U^{\max}(c_e, t_q^{(\cdot)})$ [11,27]. The considered one-dimensional flows are (i) a plug flow of constant velocity U_x and (ii) a parabolic profile $U_x(y)$ where zero velocity is shifted by a half-grid spacing outside the grid-boundary node $\mathbf{r}_b = \{\mathbf{r}_0, \mathbf{r}_N\}$. The squared velocity terms in Eq. (2) then reduce to U_x^2 terms: they remove the second-order longitudinal numerical diffusion equal to $-\Lambda^- U_x^2$ [10,11,27,26]. The modeled isotropic ADE for $C(x, y, t)$ reads

$$\partial_t C + U_x(y)\partial_x C = D_0(\partial_x^2 C + \partial_y^2 C)\ ,\ D_0 = c_e \Lambda^-\ ,\ \mathbf{U} = \{U_x, 0\}\ ,\ y \in [0, H]\ . \tag{3}$$

A scale-parameter c_e of the diffusion coefficient D_0 can be freely selected inside a $t_q^{(m)}$-dependent stability interval $]0, 1]$ [11]. Prescribing a zero-normal-flux condition on the walls: $\partial_y C|_{y=0,H} = 0$, the section-averaged concentration $\bar{C}(x, t)$ is expected to propagate with the averaged velocity $\mathcal{U}$ and to diffuse with the longitudinal coefficient $D_0(1 + k_T)$, where Taylor dispersivity $D_0 k_T$ is non-zero in the presence of the transverse velocity gradient [7,8]. In straight Poiseuille profile, one expects:

$$\partial_t \bar{C} + \mathcal{U}\partial_x \bar{C} = D\partial_x^2 \bar{C}\ ,\ D = D_0(1 + k_T)\ ,\ \bar{C}(x, t) = < C(x, y, t) > = \frac{1}{H}\int_0^H C(x, y, t)\,\mathrm{d}y\ ,$$
$$\mathcal{U} = < U_x(y) > = \frac{U_0 H^2}{12}\ ,\ U_x(y) = \frac{U_0}{2} y(H - y)\ ,\ k_T = \frac{Pe^2}{210}\ ,\ Pe = \frac{\mathcal{U}H}{c_e \Lambda^-}\ . \tag{4}$$

Starting from a Dirac delta-function $C|_{t=0} = \delta(x_0)$, numerically: $C|_{t=0} = 1$ in one grid node $x = x_0$, the first raw spatial moments $\mu_n(t) = \int_{-\infty}^{\infty}(x - x_0)^n \bar{C}(x, t)dx$ obey $\mu_1 = \mathcal{U}t$, $\mu_2 = 2Dt + \mu_1^2$. Time-independent values $\mathcal{U}^{(num)}$ and $D^{(num)}$ are computed as: $\mathcal{U}^{(num)} = (\mu_1(t + \delta t) - \mu_1(t))/\delta t$ and $D^{(num)} = (\mu_2^\star(t + \delta t) - \mu_2^\star(t))/(2\delta t)$, $\mu_2^\star = \mu_2 - \mu_1^2$.

We apply three mass-conserving boundary reflections depicted in Fig. 2: the bounce-back (d2Q9-BB), the local specular-reflection (d2Q9-SL), and the non-local, specular-forward reflection (d2Q9-SNL). These three rules reduce to d2Q5-BB on the coordinate stencil $t_c^{(a)} = t_c^{(m)} = t_c^{(u)} = \frac{1}{2}$. The d2Q5-BB and d2Q9-SNL are explored in work [26]: they produce the same solutions as for the *periodic* (mirror) conditions. In plug flow, their solutions are exact: $\mathcal{U}^{(num)} \equiv U_x$ and $D^{(num)} \equiv D_0$. In parabolic profile, they give the expected arithmetical mean velocity value: $\mathcal{U}^{(num)} = \frac{1}{H}\sum_{i=1}^{H} U_x(y_i) = \mathcal{U}(1 + \frac{1}{2H^2})$. These two schemes produce $\{t_q^{(a)}\}$-dependent, but $\{t_q^{(m)}, t_q^{(u)}\}$-independent, solution $D^{(num)} = D_0(1 + k_T + \delta k_T)$ where δk_T encompasses the numerical dispersivity of the scheme, as it is predicted [26] by combining the truncation and Taylor-dispersion analysis in parabolic flow (see Eqs. (50)–(52) there)

$$\delta k_T \approx k_T^{(1)} + k_T^{(2)}\ ,\ k_T^{(1)} = (c_e(\Lambda^-)^2 + (\Lambda - \frac{1}{4}))\frac{Pe^2}{5H^2}\ ,\ k_T^{(2)} = -3(1 - 2t_c^{(a)})(\Lambda - \frac{1}{12})\frac{Pe^2}{5H^2}\ , \tag{5}$$
$$\delta k_T \approx 0\ \text{ with }\ \Lambda(t_c^{(a)}) = \frac{t_c^{(a)}}{4(3t_c^{(a)} - 1)}\ ,\ t_c^{(a)} \in]\frac{1}{3}, \frac{1}{2}]\ ,\ \text{if } c_e(\Lambda^-)^2 \approx 0\ ,$$
$$\text{d2Q5}\ :\ \delta k_T \approx 0\ \text{ if }\ \Lambda(t_c^{(a)} = \frac{1}{2}) = \frac{1}{4}\ . \tag{6}$$

The second component $k_T^{(2)}$ vanishes in d2Q5-BB. The predicted solution (5) is in a good agreement with the numerical results obtained with d2Q9-SNL/d2Q5-BB, as can be seen in the rightmost diagram in the top row in Fig. 4 for the relative error $\mathrm{err}_D = \frac{D^{(num)}}{D} - 1 \approx \frac{\delta k_T}{1 + k_T}$. Note err_D is practically Λ-independent when $t_c^{(a)} = \frac{1}{3}$ and weight-independent when $\Lambda = \frac{1}{12}$, in agreement with Eq. (5): this expression accounts for the second-order summation effects; the exact or quasi-result has been achieved by accounting for H^{-4} and H^{-6} terms (see Eqs. (74)–(76) in [26]). In the intermediate and high-Pe range, $c_e(\Lambda^-)^2 \approx 0$ and, equating δk_T to zero, one obtains "optimal-dispersion" solution $\Lambda(t_c^{(a)})$, only existing when $t_c^{(a)} \in]\frac{1}{3}, \frac{1}{2}]$, with $\Lambda = \frac{1}{4}$ for d2Q5-BB (see results for $t_c^{(a)} = \frac{1}{2}$ in Fig. 4). The rightmost diagram in the bottom row in Fig. 4 shows the difference with the d2Q5, $\|\mathrm{err}_D(t_c^{(a)})\| = \mathrm{err}_D(t_c^{(a)}) - \mathrm{err}_D(t_c^{(a)} = \frac{1}{2})$, with $\|\mathrm{err}_D(t_c)\| \approx \frac{k_T^{(2)}}{1 + k_T}$.

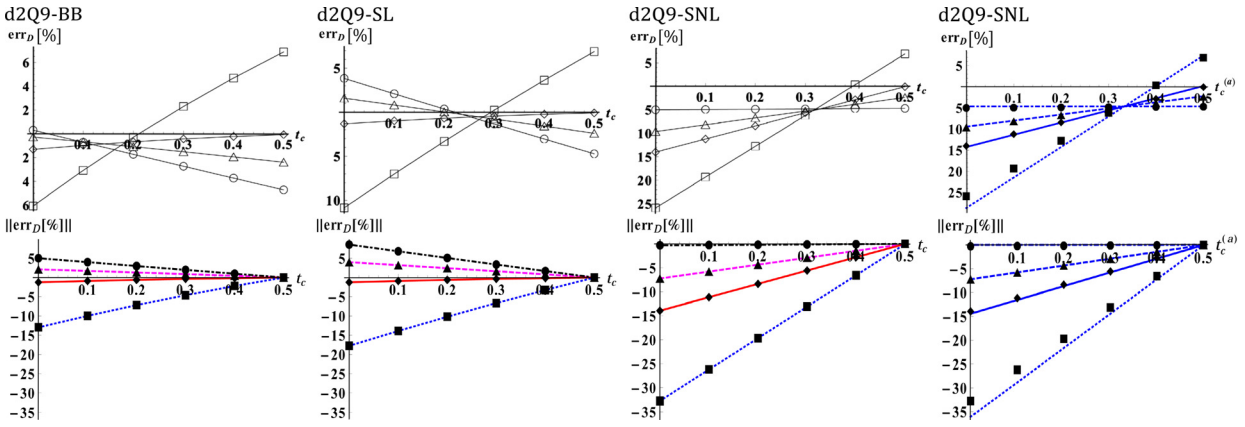

Fig. 4. (Color online.) The relative dispersion error err_D in the parabolic flow when the three coordinate weights take the same value $t_c \in [0, \frac{1}{2}]$. Top row: $\mathrm{err}_D(t_c)$ with (a) d2Q9-BB, (b) d2Q9-SL and (c) d2Q9-SNL. Bottom row: the difference with the d2Q5, $\|\mathrm{err}_D(t_c)\| = \mathrm{err}_D(t_c) - \mathrm{err}_D(t_c = \frac{1}{2})$. The truncation predictions (5) (blue lines) and d2Q9-SNL (symbols) are plotted in the last column. All results are shown for $\Lambda = \{\frac{1}{12}, \frac{1}{6}, \frac{1}{4}, \frac{1}{2}\}$ (circles, triangles, lozenges, squares).

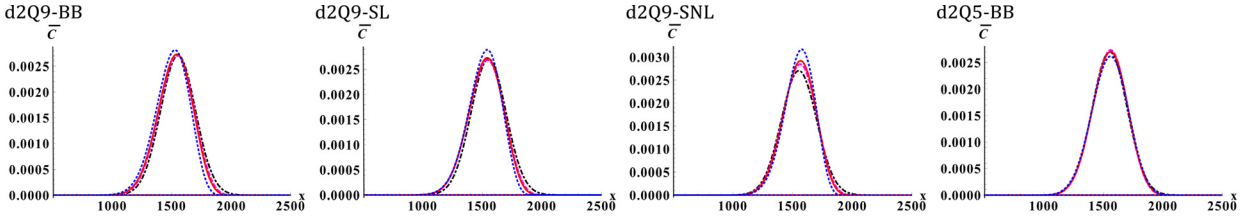

Fig. 5. (Color online.) Averaged concentration profiles in the parabolic flow of $\mathcal{U} = \frac{\sqrt{3}}{9}$ at $t = 7000$ steps are computed with the "rotated" d2Q5 and (a) BB, (b) SL, (c) SNL and (d) d2Q5-BB, with $\Lambda = \frac{1}{6}$ (dotted, magenta), $\Lambda = \frac{1}{4}$ (solid, red) and $\Lambda = \frac{1}{2}$ (dashed, blue). The analytical solution to Eq. (4) for $Pe = 80\sqrt{3}$ is dash-dotted (black).

The results with d2Q9-BB and d2Q9-SL in the first two columns in Fig. 4 are different from those with d2Q9-SNL (third column), except when they all reduce to d2Q5-BB for $t_c^{(a)} = \frac{1}{2}$. Remarkably, the d2Q9-BB and d2Q9-SL coincide for $\Lambda = \frac{1}{4}$. One might conclude, e.g., in the case of the d2Q9-BB, that the most accurate solution is reached by the "rotated" d2Q5 model $t_c = 0$, where $|\mathrm{err}_D|$ is minimum. Fig. 5 shows the averaged concentration profiles of the "rotated" d2Q5 scheme for three reflections. They confirm the dependency on Λ with d2Q9-SNL (third diagram); nevertheless, all profiles propagate here with the same (exact) velocity. This is opposed to d2Q5-BB (first diagram) and d2Q9-SL (second diagram), which both slow down the front. Finally, the d2Q5-BB results presented in the last diagram are clearly more accurate than the three solutions with the "rotated" d2Q5 model.

Similar computations conducted in plug flow are presented in Fig. 6. The d2Q5-BB and d2Q9-SNL results coincide and have equal moments (two last diagrams). At the same time, both the d2Q9-BB and d2Q9-SL completely fail: the advection velocity drastically decreases and becomes undoubtedly Λ-dependent with the BB (first diagram), while it also diminishes, but remains Λ-independent with the SL (second diagram). The two first figures in the bottom row in Fig. 6 reveal a non-uniform concentration distribution $C(y)$ with BB/SL, also illustrated by the last diagram for $\Lambda = \frac{1}{4}$. The distribution is uniform with d2Q5-BB/d2Q9-SNL (third diagram).

Fig. 7 quantifies these effects for the bounce-back. The left diagram shows the relative velocity error $\|\mathrm{err}_U(t_c)\| = \mathrm{err}_U(t_c) - \mathrm{err}_U(t_c = \frac{1}{2})$, $\mathrm{err}_U(t_c) = \frac{\mathcal{U}^{(num)}}{\mathcal{U}} - 1$ (with $\mathrm{err}_U(t_c = \frac{1}{2}) = 0$ in c-field). In c-field and p-field, only the velocity-weight $t_c^{(a)} \neq \frac{1}{2}$ modifies the advection velocity and $\mathrm{err}_U(t_c)$ is independent of velocity magnitude. The striking feature is that $\|\mathrm{err}_U\|$ decreases proportionally to $t_c^{(a)} - \frac{1}{2}$. Next, $\mathrm{err}_U(t_c)$ is negative (and therefore, the mean velocity diminishes), and $|\mathrm{err}_U(t_c)|$ increases with Λ, in agreement with the profiles in Fig. 6. The first moment confirms that in c-field, err_U is Λ-independent with the SL, and it has the same value as that of BB for $\Lambda = \frac{1}{4}$. Finally, in c-field, $\|\mathrm{err}_D(t_c)\| = \mathrm{err}_D(t_c)$ because $\mathrm{err}_D(t_c = \frac{1}{2}) = 0$. The second diagram reveals a huge non-linear increase in $\mathrm{err}_D(t_c)$ when t_c decreases from $\frac{1}{2}$ to zero. This distribution scales as $\mathcal{U}^2$, suggesting the appearance of numerical dispersion.

In summary, we observed that, in the parabolic and constant velocity fields, the d2Q9-BB and d2Q9-SL schemes with the non-zero diagonal weights modify mean advection velocity, provide non-zero diffusion error in c-field and alter truncation dispersion error in p-field. Our analysis will quantify all these effects via the separate contributions derived for three weight families. These and all other numerical solutions are illustrated for the same model parameters and the same average velocity $\mathcal{U}$ in c-field and p-field: $H = 12$, $\Lambda^- = \frac{1}{2} \times 10^{-1}$, $c_e = \frac{1}{3}$, $\mathcal{U} = 2/3 \times |U|^{\max}(c_e)/2 = \frac{\sqrt{3}}{9}$, then $Pe = 80\sqrt{3}$, with $k_T =$

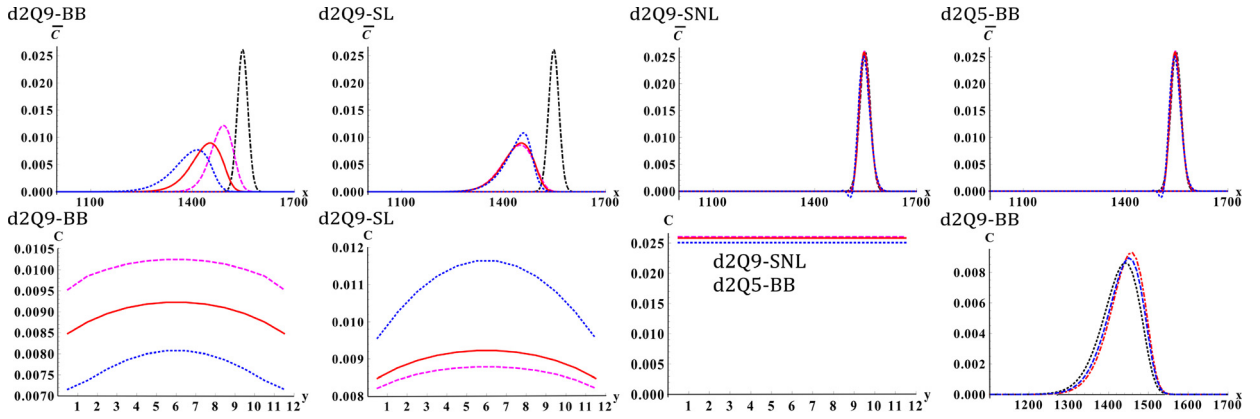

Fig. 6. (Color online.) Top row: similarly as in Fig. 5, but in plug flow where d2Q9-SNL and d2Q5-BB coincide. The analytical solution to Eq. (4) for $k_T = 0$ is dash-dotted (black line). Bottom row: three first diagrams show the corresponding dependency $C(y)$ at the x-point where $\bar{C}$ is maximum. The last diagrams plots BB/SL solutions with $\Lambda = \frac{1}{4}$ at the boundary nodes $y = 0.5$ (dotted, black), at the center of the channel (dot-dashed, red) and the average solution (dashed blue).

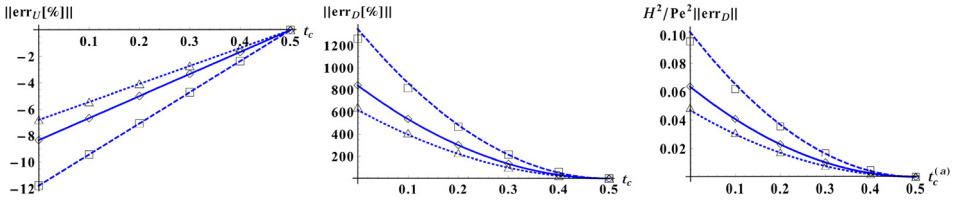

Fig. 7. (Color online.) The d2Q9-BB in plug flow. The two first diagrams show the relative differences with the d2Q5 in advection velocity ($\|\mathrm{err}_U(t_c)\| = \mathrm{err}_U(t_c)$) and diffusion coefficient ($\|\mathrm{err}_D(t_c)\| = \mathrm{err}_D(t_c)$) when all weights take the same value $t_c = t_c^{(m)} = t_c^{(a)} = t_c^{(u)}$, for $\Lambda = \frac{1}{6}$ ("triangles"), $\Lambda = \frac{1}{4}$ ("lozenges"), $\Lambda = \frac{1}{2}$ ("squares"). The lines depict the analytical predictions, with Eq. (24) for $\mathrm{err}_U(t_c^{(a)}) = \delta\mathcal{U}^{(a)}$ and a sum of three contributions for $\mathrm{err}_D = \delta D_0^{(m)} + \delta D_0^{(u)} + k_T^{(a)}$, obtained from Eqs. (19), (20) and (29). The last diagram plots (rescaled) dispersivity coefficient (29).

91.4286 in p-field and $k_T = 0$ in c-field. This choice of velocity halves in the p-field the maximum stable (two-dimensional) velocity amplitude $|U|^{\max} = \min\{\sqrt{2c_e}, \sqrt{1-2c_e}\}$ of the d2Q5 scheme [11].

3. Non-equilibrium boundary layers

This section is based on the *steady-state recurrence equations* of the TRT scheme derived in Ref. [20]. They present two pairs of exact linear combinations of the evolution equation (1), where the time variable is dropped:

$$\begin{cases} g_q^{\pm}(\mathbf{r}) = [\bar{\Delta}_q e_q^{\mp} - \Lambda^{\mp}\bar{\Delta}_q^2 e_q^{\pm} + (\Lambda - \frac{1}{4})\bar{\Delta}_q^2 g_q^{\pm}](\mathbf{r})\,, & \text{(a)} \\ [\bar{\Delta}_q^2 e_q^{\pm} - \Lambda^{\pm}\bar{\Delta}_q^2 g_q^{\pm} - \bar{\Delta}_q g_q^{\mp}](\mathbf{r}) = 0\,, & \text{(b)} \end{cases} \tag{7}$$

with $\bar{\Delta}_q\psi(\mathbf{r}) = \frac{1}{2}(\psi(\mathbf{r}+\mathbf{c}_q) - \psi(\mathbf{r}-\mathbf{c}_q))$ and $\bar{\Delta}_q^2\psi(\mathbf{r}) = \psi(\mathbf{r}+\mathbf{c}_q) - 2\psi(\mathbf{r}) + \psi(\mathbf{r}-\mathbf{c}_q)$, $\forall\,\psi$. By construction, these equations are only valid for those links where all populations are issued from the propagation step. In form of the infinite series for g_q around e_q, the solution to Eqs. (7) has the same coefficients as the steady-state Chapman–Enskog expansion [20]. The recurrence equations remain satisfied if we disturb $g_q^{\pm}(\mathbf{r})$ by the following correction $\delta g_q^{\pm}(\mathbf{r})$:

$$\begin{cases} \delta g_q^{\pm}(\mathbf{r}) = (\Lambda - \frac{1}{4})\bar{\Delta}_q^2 \delta g_q^{\pm}(\mathbf{r})\,, & \text{(a)} \\ [\Lambda^{\pm}\bar{\Delta}_q^2 \delta g_q^{\pm} + \bar{\Delta}_q \delta g_q^{\mp}](\mathbf{r}) = 0\,. & \text{(b)} \end{cases} \tag{8}$$

This correction, referred to as *non-equilibrium boundary layer*, will allow us to couple the expected bulk solution, obeying the Chapman–Enskog expansion, to the closure relation of the boundary scheme. In order to construct $\delta g_q^{\pm}(\mathbf{r})$, let us consider grid nodes $\mathbf{r}_n = \mathbf{r}_0 + n\mathbf{c}_q$ along lattice direction $\mathbf{c}_q$, from one boundary end at $\mathbf{r} = \mathbf{r}_0$ to another at $\mathbf{r}_N = \mathbf{r}_0 + N\mathbf{c}_q$ (see Fig. 8). According to Eq. (8)(a), $\delta g_q^{\pm}(\mathbf{r}) \neq 0$ when $\Lambda = \frac{1}{4}$ only in two boundary nodes $\mathbf{r}_b = \{\mathbf{r}_0, \mathbf{r}_N\}$. When $\Lambda \neq \frac{1}{4}$, the solution to Eqs. (8) has the form $\delta g_q^{\pm}(\mathbf{r}_n) = a_q^{\pm}k_\sigma^n + b_q^{\pm}k_\sigma^{-n}$, where $\{a_q^{\pm}, b_q^{\pm}\}$ are linkwise-constant and k_σ has two roots:

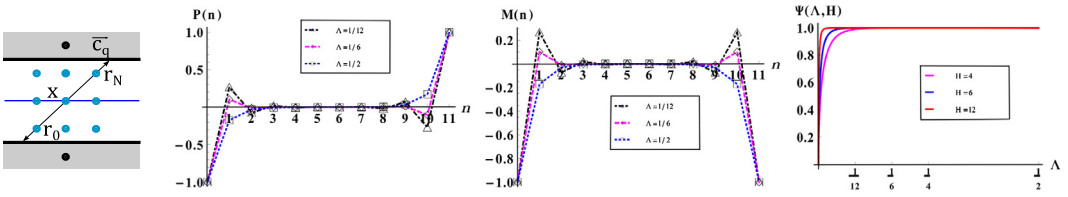

Fig. 8. (Color online.) First diagram provides notations for boundary-layer analysis. Second and third diagrams plot functions $P(n)$ and $M(n)$ from Eq. (11) in a channel of $H=12$ for $\Lambda=\frac{1}{12}$ ("triangles", magenta), $\Lambda=\frac{1}{6}$ ("lozenges", blue), $\Lambda=\frac{1}{2}$ ("squares", red). Last diagram plots function $\Psi(\Lambda,H)$ versus Λ when $H=\{4,6,12\}$ (solid, dashed, dotted).

$$\begin{cases} \Lambda\neq\dfrac{1}{4} & : \ k_\sigma=\dfrac{2\sqrt{\Lambda}-\sigma}{2\sqrt{\Lambda}+\sigma}\ ,\ \sigma=\pm1\ ,\ \sqrt{\Lambda^+}a_q^+=\sigma\sqrt{\Lambda^-}a_q^-\ ,\ \sqrt{\Lambda^+}b_q^+=-\sigma\sqrt{\Lambda^-}b_q^-\ , \quad \text{(a)} \\ \Lambda=\dfrac{1}{4} & : \ \delta g_q^\mp(\mathbf{r}_0)=\dfrac{\delta g_q^\pm(\mathbf{r}_0)}{2\Lambda^\mp}\ ,\ \delta g_q^\mp(\mathbf{r}_N)=-\dfrac{\delta g_q^\pm(\mathbf{r}_N)}{2\Lambda^\pm}\ ,\ \text{with}\ 2\Lambda^\mp=\dfrac{1}{2\Lambda^\pm}\ . \quad \text{(b)} \end{cases} \tag{9}$$

The above relations between different parity components are obtained from Eq. (8)(b). We assume that $k=k_1$ ($\sigma=1$), then $|k|<1$ and solution of Eqs. (8) with Eq. (9)(a), obeying prescribed boundary values $\delta g_q^+(n=0)=\delta g_q^+(\mathbf{r}_0)$ and $\delta g_q^+(n=N)=\delta g_q^+(\mathbf{r}_N)$, reads

$$\delta g_q^+(\mathbf{r}_n)=p_N(n)\delta g_q^+(\mathbf{r}_N)+p_0(n)\delta g_q^+(\mathbf{r}_0)\ ,\ p_N(n)=\frac{k^n-k^{-n}}{k^N-k^{-N}}\ ,\ p_0(n)=\frac{k^{(N-n)}-k^{-(N-n)}}{k^N-k^{-N}}\ . \tag{10}$$

Now, we make use of the axial symmetry in the straight channel. The first possible situation is $\delta g_q^+(\mathbf{r}_N)=-\delta g_q^+(\mathbf{r}_0)$, then $\delta g_q^-(\mathbf{r}_N)=\delta g_q^-(\mathbf{r}_0)$ and Eq. (10) becomes

$$\begin{cases} \delta g_q^+(\mathbf{r}_n)=P(n)\delta g_q^+(\mathbf{r}_N)\ , & P(n)=\dfrac{k^n-k^{(N-n)}}{k^N-1}\ ,\ P(N)=-P(0)=1\ , \quad \text{(a)} \\ \delta g_q^-(\mathbf{r}_n)=\dfrac{\sqrt{\Lambda}}{\Lambda^-}M(n)\delta g_q^+(\mathbf{r}_N)\ , & M(n)=\dfrac{k^n+k^{(N-n)}}{k^N-1}\ ,\ M(N)=M(0)=\dfrac{k^N+1}{k^N-1}\ . \quad \text{(b)} \end{cases} \tag{11}$$

The functions $P(n)$ and $M(n)$ are plotted in Fig. 8: they monotonously decay towards the center when $\Lambda>\frac{1}{4}$ but oscillate when $\Lambda<\frac{1}{4}$. When $\Lambda=\frac{1}{4}$, they are constrained to boundary nodes. By symmetry, $<P(n)>=0$ but we will need the auxiliary functions $\psi(\Lambda,H)$ and $\Psi(\Lambda,H)$ of $<M(n)>$:

$$\begin{aligned} &\psi(\Lambda,H)=-\frac{<M(n)>H}{2\sqrt{\Lambda}-M(N)}=1\ ,\ <M(n)>=\frac{\sum_{n=0}^{N=H-1}M(n)}{H}=\frac{1}{H}(1-2\sqrt{\Lambda}+\frac{2}{k^N-1})\ , \\ &\Psi(\Lambda,H)=-\frac{<M(n)>H}{1-2\sqrt{\Lambda}M(N)}=(\frac{2}{1+k^{N+1}}-1)\ ,\ \Psi(H)|_{\Lambda=\frac{1}{4}}=\Psi(\Lambda)|_{H\to\infty}=1\ . \end{aligned} \tag{12}$$

Fig. 8 shows that $\Psi(\Lambda,H)$ rapidly approaches its asymptotic value $\Psi|_{H\to\infty}=1$ when $\Lambda>0$, and it vanishes when $\Lambda\to0$.

A second possible situation is $\delta g_q^+(\mathbf{r}_N)=\delta g_q^+(\mathbf{r}_0)$, then $\delta g_q^-(\mathbf{r}_N)=-\delta g_q^-(\mathbf{r}_0)$:

$$\begin{cases} \delta g_q^-(\mathbf{r}_n)=\dfrac{\sqrt{\Lambda}}{\Lambda^-}\mathcal{M}(n)\delta g_q^+(\mathbf{r}_N)\ ,\ \mathcal{M}(n)=\dfrac{k^n-k^{(N-n)}}{k^N+1}\ ,\ \mathcal{M}(N)=-\mathcal{M}(0)=\dfrac{k^N-1}{k^N+1}\ , \quad \text{(a)} \\ \delta g_q^+(\mathbf{r}_n)=\mathcal{P}(n)\delta g_q^+(\mathbf{r}_N)\ , \quad \mathcal{P}(n)=\dfrac{k^n+k^{(N-n)}}{k^N+1}\ ,\ \mathcal{P}(N)=\mathcal{P}(0)=1\ . \quad \text{(b)} \end{cases} \tag{13}$$

The averaged functions obey: $<\mathcal{M}(n)>=0$ and $\Phi(\Lambda,H)=\frac{<\mathcal{P}(n)>H}{2\sqrt{\Lambda}-\mathcal{M}(N)}=\Psi(\Lambda,H)$, with

$$\phi(\Lambda,H)=\frac{<\mathcal{P}(n)>H}{1-2\sqrt{\Lambda}\mathcal{M}(N)}=1\ ,\ <\mathcal{P}(n)>=\frac{1}{H}(1-2\sqrt{\Lambda}+\frac{4\sqrt{\Lambda}}{k^N-1})\ . \tag{14}$$

In order to closure the system for $\delta g_q^+(\mathbf{r}_N)$, one has to provide a boundary rule, e.g., the bounce-back (BB) rule reads at steady-state for cut link q:

$$\text{BB}: f_{\bar{q}}(\mathbf{r}_b)=(f_q+g_q^++g_q^-)(\mathbf{r}_b)\ ,\ \text{if}\ \mathbf{r}_b+\mathbf{c}_q\in\text{solid}. \tag{15}$$

Replacing $f_q(\mathbf{r}_b)$ by $(e_q^++e_q^-)-(\Lambda^++\frac{1}{2})g_q^+-(\Lambda^-+\frac{1}{2})g_q^-$, and using decomposition $g_q^\pm=G_q^\pm+\delta g_q^\pm$ into "bulk" ($G_q^\pm$) and "boundary-layer" ($\delta g_q^\pm$) components, the closure relation of the bounce-back reads:

$$\text{BB}: [e_q^- + \frac{1}{2}(G_q^+ + \delta g_q^+) - \Lambda^-(G_q^- + \delta g_q^-)]|_{\mathbf{r}_b} = 0\,. \tag{16}$$

Prescribing the expected bulk solution for $G_q^{\pm}$ and Eqs. (11) or Eqs. (13) for $\delta g_q^{\pm}$, we will derive $\delta g_q^{\pm}(\mathbf{r}_N)$ from the closure relation (16), then construct boundary layers and, finally, estimate their impact on the averaged transport coefficients, with the help of Eqs. (12) and (14).

4. Impact of the "spurious" boundary layers

In Section 4.1, we first derive the exact, velocity-independent correction to diffusion coefficient due to the diagonal mass-weight $t_q^{(m)}$, then extend it to U_x^2-weight $t_q^{(u)}$ in Section 4.2. The exact correction of the velocity field, due to the velocity-weight $t_q^{(a)}$, is constructed in Section 4.3. The associated longitudinal dispersion is derived in Section 4.4. The individual diffusion and dispersion corrections can be summed for three weight families. The details are provided for the bounce-back rule, an extension for other boundary conditions is almost straightforward. All results are compared with the numerical simulations in plug and parabolic flows.

4.1. Bounce-back diffusion-coefficient correction due to the mass-weight $t_q^{(m)}$

When the coordinate mass-weight $t_c^{(m)}$ varies from $\frac{1}{2}$ to 0, the diagonal links obtain non-zero component $e_q^+ = t_d^{(m)} c_e C$, $t_d^{(m)} \in [0, \frac{1}{4}]$. Naturally, the mass weight only affects the diffusion coefficient: $D_0 = c_e\Lambda^- \to c_e\Lambda^-(1 + \delta D_0^{(m)}(t_c^{(m)}))$ in Eq. (4). Hence, the correction $\delta D_0^{(m)}(t_c^{(m)})$ is velocity independent and the same as in pure diffusion case. According to the Chapman–Enskog analysis and in agreement with Eq. (7)(a), one expects a y-independent, second-order pure-diffusion solution as: $G_q^- = t_q^{(m)} c_e \bar{\Delta}_x \bar{\mathcal{C}}(x,t) c_{qx}$, $G_q^+ = -\Lambda^- \bar{\Delta}_q G_q^- = -\Lambda^- t_q^{(m)} c_e \Delta_x^2 \bar{\mathcal{C}}(x,t) c_{qx}^2$. This last term gives the isotropic diffusion term in the RHS of the modeled mass-conservation equation (4), with $-\sum_{q=0}^{Q_m} G_q^+ = \Lambda^- c_e \Delta_x^2 \bar{\mathcal{C}}(x,t)$. However, the diagonal cut links should obey the bounce-back closure relation (16). Firstly, let us assume $\delta g_q^{\pm} = 0$. Since $e_q^- = 0$, the difference of Eqs. (16) for two cut diagonal-links yields: $-2\Lambda^- c_e t_d^{(m)} \bar{\Delta}_x \bar{\mathcal{C}}(x,t)(\mathbf{r}_N) = 0$. It means that the bounce-back enforces zero tangential boundary flux when $t_d^{(m)} \neq 0$. The incompatibility with the bulk solution causes an appearance of the accommodation correction (11) in the form:

$$\delta g_q^+(\mathbf{r}_n) = k_1 P(n) \bar{\Delta}_x \bar{\mathcal{C}}(x,t) c_{qx} c_{qy}\,,\ \delta g_q^-(\mathbf{r}_n) = \frac{\sqrt{\Lambda}}{\Lambda^-} k_1 M(n) \bar{\Delta}_x \bar{\mathcal{C}}(x,t) c_{qx} c_{qy}^2\,. \tag{17}$$

It satisfies Eqs. (8) with $\bar{\Delta}_q = \bar{\Delta}_y c_{qy}$, $\bar{\Delta}_q^2 = \Delta_y^2 c_{qy}^2$, $\delta g_q^+(\mathbf{r}_N) = k_1 \bar{\Delta}_x \bar{\mathcal{C}}(x,t) c_{qx} c_{qy}$; the x-coordinate is assumed to be set by the point where lattice direction along $\mathbf{c}_q$, from $\mathbf{r}_0$ to $\mathbf{r}_N = \mathbf{r}_0 + N\mathbf{c}_q$, cuts the channel axis $y = H/2$ (see Fig. 8). To find k_1, we substitute $G_q^- = t_q^{(m)} c_e \bar{\Delta}_x \bar{\mathcal{C}}(x,t) c_{qx}$, $G_q^+ = -\Lambda^- t_q^{(m)} c_e \Delta_x^2 \bar{\mathcal{C}}(x,t) c_{qx}^2$ together with Eq. (17) into Eq. (16) and consider their difference for two diagonal links. This gives

$$[k_1 P(N) - 2\Lambda^-(t_d^{(m)} c_e + k_1 \frac{\sqrt{\Lambda}}{\Lambda^-} M(N))] \bar{\Delta}_x \bar{\mathcal{C}}(x,t) = 0 \text{ then } k_1 = \frac{2\Lambda^- c_e t_d^{(m)}}{1 - 2\sqrt{\Lambda} M(N)}\,. \tag{18}$$

The correction to the averaged diffusion term is expected as $\Lambda^- < \sum_{q=1}^{Q_m} \bar{\Delta}_x \delta g_q^- c_{qx} >$. Substituting Eq. (17) yields this correction as: $\Lambda^- k_1 \frac{\sqrt{\Lambda}}{\Lambda^-} < M(n) > \Delta_x^2 \bar{\mathcal{C}}(x,t) \sum_{q=0}^{Q_m} c_{qx}^2 c_{qy}^2$, with $\sum_{q=1}^{Q_m} c_{qx}^2 c_{qy}^2 = 4$. Now we substitute Eq. (18) for k_1 and employ Eq. (12) to express $< M(n) >$, using $t_d^{(m)} = \frac{1 - 2t_c^{(m)}}{4}$. The contribution $c_e\Lambda^- \delta D_0^{(m)}$ to diffusion coefficient $D_0 = c_e\Lambda^-$ from the correction $4k_1\sqrt{\Lambda} < M(n) >$ reads:

$$\begin{cases} \delta D_0^{(m)} = -2\sqrt{\Lambda} \dfrac{(1 - 2t_c^{(m)})}{H} \Psi(\Lambda, H)\,,\ \forall\, H \geq 2\,, & \text{(a)} \\ \delta D_0^{(m)} = -\dfrac{(1 - 2t_c^{(m)})}{H}\,,\ \text{if } \Lambda = \dfrac{1}{4}\,,\ \forall\, H \geq 2\,, & \text{(b)} \\ \delta D_0^{(m)}|_{H\to\infty} = -2\sqrt{\Lambda} \dfrac{(1 - 2t_c^{(m)})}{H}\,,\ \forall\, \Lambda\,. & \text{(c)} \end{cases} \tag{19}$$

This solution predicts that D_0 is diminished by $\delta D_0^{(m)} D_0$. This last quantity decays with Λ towards zero and it vanishes for $t_c^{(m)} = \frac{1}{2}$, $\forall\Lambda$. Asymptotically, $\delta D_0^{(m)}$ behaves as the first-order relative correction $-2\sqrt{\Lambda}(1 - 2t_c^{(m)})/H$, while $\Lambda = \frac{1}{4}$ produces this solution for any H. Fig. 9 confirms that the numerical results for $(1 + k_T)\|\text{err}_D(t_c^{(m)})\|$ coincide with the prescribed function $\|\text{err}_D\| = \delta D_0^{(m)}(t_c^{(m)})$ in c-field (left diagram) and in p-field (middle diagram). Since amplitude of $\|\text{err}_D\|$ decreases as $1/(1 + k_T)$ when Pe increases, the largest boundary-layer impact happens for pure diffusion and in c-field, because

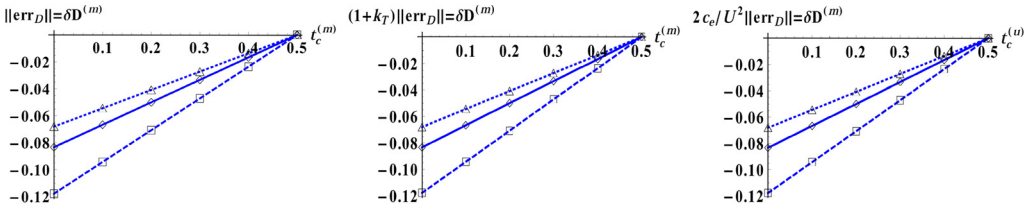

Fig. 9. (Color online.) The d2Q9-BB model with $\Lambda=\frac{1}{6}$ ("triangles"), $\Lambda=\frac{1}{4}$ ("lozenges"), $\Lambda=\frac{1}{2}$ ("squares"). The left and middle diagrams plot numerical results for $(1+k_T)\|\mathrm{err}_D(t_c^{(m)})\|$ and analytical predictions (19) (lines) in c-field (where $k_T=0$) and p-field, respectively. Last diagram plots (rescaled) results for $\|\mathrm{err}_D(t_c^{(u)})\|$ and prediction (20) (lines) in c-field.

$k_T=0$. Fig. 11 (left diagram) presents $\|\mathrm{err}_D(t_c^{(m)})\|$ for computations with the background p-field, similar as in Fig. 4, but when only the mass weight varies. Fig. 11 shows that the local specular reflection produces very similar linear dependency $\|\mathrm{err}_D(t_c^{(m)})\|$, but of slightly smaller amplitude; the two reflections coincide for $\Lambda=\frac{1}{4}$. Still, in either c-field or p-field, as $\delta D_0^{(m)}$ is negative, this cannot explain the observed increase of the apparent diffusion coefficient in Figs. 4 and 7 (reported there for case when all three weights vary together). The next sections explore the additional sources for that.

4.2. Bounce-back diffusion-coefficient correction due to the U_x^2-weight $t_q^{(u)}$

In a one-dimensional velocity field, the anti-numerical-diffusion correction in Eq. (2) reduces to $\frac{1}{2}t_q^{(u)}U_x^2C$. In c-field, this term is link-wise constant and its correction to the diffusion coefficient can be obtained similarly as for the mass term $t_q^{(m)}c_eC$ in Eqs. (19), by only replacing there c_e by $U_x^2/2$ and $t_c^{(m)}$ by $t_c^{(u)}$. In variable velocity field U_x^2 varies along the link and one may expect to get the same functional form as in c-field only for $\Lambda=\frac{1}{4}$, replacing c_e by *boundary value* $U_x^2(\mathbf{r}_b)/2$. Therefore, in plug flow or when $\Lambda=\frac{1}{4}$, the relative correction $\delta D_0^{(u)}$ to the diffusion coefficient coming from $t_q^{(u)}$-weight is expected as:

$$\begin{cases} \delta D_0^{(u)} = -\sqrt{\Lambda}\dfrac{U_x^2(\mathbf{r}_b)}{c_e}\dfrac{(1-2t_c^{(u)})}{H}\Psi(\Lambda,H)\,,\ \forall\, H\geq 2\,, & \text{(a)} \\ \delta D_0^{(u)} = -\dfrac{U_x^2(\mathbf{r}_b)}{2c_e}\dfrac{(1-2t_c^{(u)})}{H}\ \text{if}\ \Lambda=\dfrac{1}{4}\,,\ \forall\, H\geq 2\,, & \text{(b)} \\ \delta D_0^{(u)}|_{H\to\infty} = -\sqrt{\Lambda}\dfrac{U_x^2(\mathbf{r}_b)}{c_e}\dfrac{(1-2t_c^{(u)})}{H}\,,\forall\,\Lambda\,. & \text{(c)} \end{cases} \tag{20}$$

The numerical simulations in Fig. 9 (last diagram) confirm that, when only the $t_q^{(u)}$-weight is different from $\frac{1}{2}$, $\|\mathrm{err}_D\|=\delta D_0^{(u)}$ with $U_x^2(\mathbf{r}_N)\equiv U_x^2$ in c-field, and $(1+k_T)\|\mathrm{err}_D\|=\delta D_0^{(u)}$ for $\Lambda=\frac{1}{4}$ in p-field. When $\Lambda\neq\frac{1}{4}$, the additional effect due to the velocity variation in p-field will be considered in Section 4.3. Indeed, the diffusion correction due to the U_x^2-term is negligible in p-field because the velocity amplitude in square is small in the boundary nodes. Fig. 11 (middle diagram) illustrates this by showing that the respective role of $t_q^{(u)}$-correction in p-field is much less significant than the diffusion term due to $t_q^{(m)}$, because $U_x^2(\mathbf{r}_b)<<c_e$.

In summary, the amplitude of the diffusion-coefficient correction due to the diagonal weights of the anti-numerical-diffusion terms is much less significant in a variable velocity field than in a plug flow of the same average amplitude. Furthermore, in a variable velocity field, this correction is dominated by the mass-weight correction. The two corrections act independently and can be summed for any individual choice of these two weight families.

4.3. Bounce-back velocity correction due to velocity weight $t_q^{(a)}$

The two families of weights $\{t_q^{(m)},t_q^{(u)}\}$ do not modify the velocity profile and produce the same mean velocity with the bounce-back and local specular reflection as the d2Q9-BB and d2Q9-SNL. This situation changes when the diagonal velocity weight $t_d^{(a)}$ becomes non-zero and the advection front slows down, as illustrated in Figs. 5 and 6. This effect is quantified in this section.

4.3.1. Constant velocity field and Poiseuille profile with $\Lambda=\frac{1}{4}$

When the coordinate velocity weight $t_c^{(a)}$ varies from $\frac{1}{2}$ to 0, the diagonal links in Eq. (2) obtain non-zero components $e_q^-=t_q^{(a)}U_xCc_{qx}$ with $t_d^{(a)}\in[0,\frac{1}{4}]$. This situation is very similar to the restriction of the tangential diffusion flux quantified in Section 4.1, because now the bounce-back closure relation (16) enforces U_x to zero. The boundary layer correction $\delta g_q^{\pm}$ accommodates this deficiency. Following Eq. (17), we suggest $\delta g_q^{\pm}$ in the form:

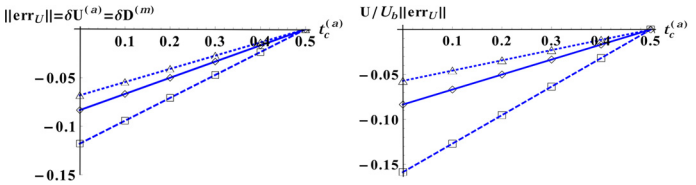

Fig. 10. (Color online.) The d2Q9-BB with the c-field (left diagram) and p-field (right diagram), when $\Lambda=\frac{1}{6}$ ("triangles"), $\Lambda=\frac{1}{4}$ ("lozenges"), $\Lambda=\frac{1}{2}$ ("squares"). The two diagrams plot the rescaled relative velocity error $\mathcal{U}/U_b\|\mathrm{err}_U(t_c^{(a)})\|$, with $\mathcal{U}/U_b=1$ and $U_b=U_x(\mathbf{r}_\mathrm{b})$, respectively. The analytical predictions (lines) for $\delta\mathcal{U}^{(a)}$ are exact and respectively given by Eqs. (24)(a) and (26).

$$\delta g_q^+(\mathbf{r}_n)=k_1P(n)\bar{\mathcal{C}}(x,t)c_{qx}c_{qy}\ ,\ \delta g_q^-(\mathbf{r}_n)=\frac{\sqrt{\Lambda}}{\Lambda^-}k_1M(n)\bar{\mathcal{C}}(x,t)c_{qx}c_{qy}^2\ . \tag{21}$$

Substituting Eq. (21) into Eq. (16), the difference of these closure relations for two diagonal-links gives with $G_q^{\pm}=0$:

$$U_x=const\ :\ \bar{\mathcal{C}}(x,t)(2t_d^{(a)}U_x(\mathbf{r}_\mathrm{b})+k_1(1-2\sqrt{\Lambda}M(N))=0\ ,\ \text{ then }\ k_1=-\frac{2t_d^{(a)}U_x(\mathbf{r}_\mathrm{b})}{1-2\sqrt{\Lambda}M(N)}\ . \tag{22}$$

Now we expect the term $-\Lambda^-\sum_{q=1}^{Q_m}\bar{\Delta}_x\delta g_q^-c_{qx}$ to modify the convective flux in the LHS of Eq. (3) by a quantity $\delta U^{(a)}(n)\mathcal{U}\bar{\Delta}_x\bar{\mathcal{C}}(x,t)$, where the relative velocity correction $\delta U^{(a)}(n)$ leads to the following solution in c-field:

$$U_x=const\ :\ \delta U^{(a)}(n)=\frac{2\sqrt{\Lambda}(1-2t_c^{(a)})M(n)}{1-2\sqrt{\Lambda}M(N)}\frac{U_x(\mathbf{r}_\mathrm{b})}{\mathcal{U}}\ , \tag{23}$$

with $U_x(\mathbf{r}_\mathrm{b})/\mathcal{U}=1$ in c-field. The mean velocity $\mathcal{U}$ obtains correction $\delta\mathcal{U}^{(a)}\mathcal{U}$ with $\delta\mathcal{U}^{(a)}$ given as:

$$\begin{cases}\delta\mathcal{U}^{(a)}=<\delta U^{(a)}(n)>=-2\sqrt{\Lambda}\dfrac{(1-2t_c^{(a)})}{H}\dfrac{U_x(\mathbf{r}_\mathrm{b})}{\mathcal{U}}\Psi(\Lambda,H)\ ,\ \forall\ H\geq 2\ , & \text{(a)}\\ \delta\mathcal{U}^{(a)}=-\dfrac{(1-2t_c^{(a)})}{H}\dfrac{U_x(\mathbf{r}_\mathrm{b})}{\mathcal{U}}\ ,\ \text{if }\ \Lambda=\dfrac{1}{4}\ ,\ \forall\ H\geq 2\ , & \text{(b)}\\ \delta\mathcal{U}^{(a)}|_{H\to\infty}=-2\sqrt{\Lambda}\dfrac{(1-2t_c^{(a)})}{H}\dfrac{U_x(\mathbf{r}_\mathrm{b})}{\mathcal{U}}\ ,\ \forall\ \Lambda\ . & \text{(c)}\end{cases} \tag{24}$$

We emphasize that $\delta\mathcal{U}^{(a)}(t_c^{(a)})$ is independent of the velocity amplitude and it presents the same function of the weight value $t_c^{(a)}$ as $\delta D_0^{(m)}(t_c^{(m)})$. This solution predicts linear with $\frac{1}{2}-t_c^{(a)}$ decay for mean velocity amplitude; it decreases as the *first-order* correction with H and it reduces as $\sqrt{\Lambda}$. Fig. 10 (left diagram) confirms that the numerical results for $\|\mathrm{err}_U\|=\mathrm{err}_U(t_c^{(a)})$ in c-field *coincide* with the predicted solution (24). Furthermore, solution (24)(b) derived for $\Lambda=\frac{1}{4}$ is valid for any Λ in c-field when applying local specular reflection (SL). The second diagram in Fig. 10 displays that it also remains valid in parabolic profile for $\Lambda=\frac{1}{4}$. Since velocity correction (24) scales with prefactor $\frac{U_x(\mathbf{r}_\mathrm{b})}{\mathcal{U}}<<1$, the retardation of the front is much less significant in parabolic profile, which is in agreement with the average concentration profiles depicted in Figs. 5 and 6.

4.3.2. Parabolic velocity field

One should take into account the velocity variation along the diagonal links for the construction of a boundary layer in the parabolic profile. Including the first- and second-order velocity derivatives into Chapman–Enskog component $G_q^{\pm}$, the velocity deviation $\mathcal{U}\delta U^{(a)}(n)$ reads:

$$\begin{aligned}&\mathrm{BB}\ :\ \mathcal{U}\delta U^{(a)}(n)=-4\sqrt{\Lambda}k_1M(n)-4k_2\mathcal{P}(n)\ ,\ \text{with}\\ &k_1=-\frac{2t_d^{(a)}}{1-2\sqrt{\Lambda}M(N)}(U_x-\frac{1}{2}|\partial_yU_x|+\Lambda\partial_y^2U_x)|_{\mathbf{r}_\mathrm{b}}\ ,\\ &k_2=\frac{2t_d^{(a)}\Lambda}{1-2\sqrt{\Lambda}\mathcal{M}(N)}(|\partial_yU_x|-\frac{1}{2}\partial_y^2U_x)|_{\mathbf{r}_\mathrm{b}}\ .\end{aligned} \tag{25}$$

This solution reduces to Eq. (23) for constant velocity. The averaged velocity $\mathcal{U}$ gets the relative correction $\delta\mathcal{U}^{(a)}=<\delta U^{(a)}(n)>$, which reads with the help of Eqs. (12) and (14):

$$\begin{cases}\delta\mathcal{U}^{(a)}=-\dfrac{2(1-2t_c^{(a)})\sqrt{\Lambda}}{H\mathcal{U}}((U_x-\dfrac{1}{2}|\partial_yU_x|+\Lambda\partial_y^2U_x)\Psi(\Lambda,H)-\sqrt{\Lambda}(-|\partial_yU_x|+\dfrac{1}{2}\partial_y^2U_x))|_{\mathbf{r}_\mathrm{b}}\ , & \text{(a)}\\ \delta\mathcal{U}^{(a)}=-\dfrac{(1-2t_c^{(a)})}{H}\dfrac{U_x(\mathbf{r}_\mathrm{b})}{\mathcal{U}}\ ,\ \text{if }\ \Lambda=\dfrac{1}{4}\ . & \text{(b)}\end{cases} \tag{26}$$

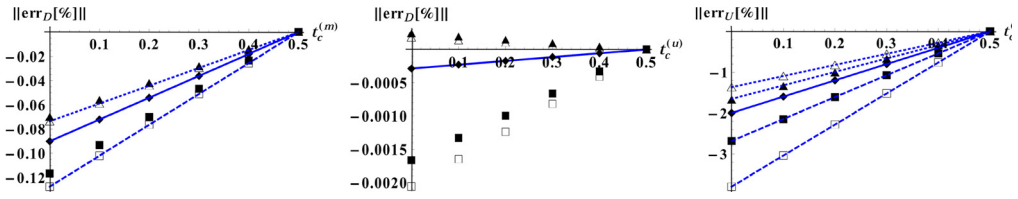

Fig. 11. (Color online.) These three diagrams depict $\|\mathrm{err}_D(t_c^{(m)})\|$, $\|\mathrm{err}_D(t_c^{(u)})\|$ and $\|\mathrm{err}_U(t_c^{(a)})\|$ in parabolic profile, with empty symbols for BB and black symbols for SL. The analytical predictions (blue lines) are exact in BB, with Eq. (19) for $\|\mathrm{err}_D(t_c^{(m)})\|$, Eq. (20) for $\|\mathrm{err}_D(t_c^{(u)})\|$ when $\Lambda = \frac{1}{4}$ and Eq. (26) for $\|\mathrm{err}_U(t_c^{(a)})\|$.

Since $\Psi(\Lambda, H)|_{\Lambda=\frac{1}{4}} = 1$, this solution reduces to Eq. (24)(b) for $\Lambda = \frac{1}{4}$. The second diagram in Fig. 10 demonstrates that solution (26) exactly describes $\|\mathrm{err}_U(t_c^{(a)})\|$; these values are rescaled with $U_x(\mathbf{r}_b)/\mathcal{U}$ to allow for the comparison with the c-field results displayed in the left diagram. The numerical computations correspond to Fig. 4 and $\|\mathrm{err}_U(t_c^{(a)})\|$ (in percents) is plotted again in Fig. 11 together with the numerical results and the approximate solution for d2Q9-SL. As in the c-field, d2Q9-BB and d2Q9-SL produce the same velocity correction when $\Lambda = \frac{1}{4}$. Otherwise, the deviation from $\Lambda = \frac{1}{4}$ is weaker in SL, which is in agreement with Fig. 5.

4.4. Bounce-back dispersion correction due to the velocity weight $t_q^{(a)}$

The idea is to construct the longitudinal numerical dispersion due to the transverse gradients in the induced velocity profiles (23) and (25). The purpose is to verify whether it explains the large increase in the diffusion coefficient reported in Figs. 7 and 4, respectively. Recall that the negative diffusion corrections due to the weights $\{t_d^{(m)}, t_d^{(u)}\}$ could not explain these results.

4.4.1. Constant velocity

Following Taylor's idea, the solute distribution $C(x, y, t)$ and the apparent velocity field $u_x(y)$ are disturbed around their cell-averaged values $\bar{C}(x, t)$ and $\tilde{\mathcal{U}}$, respectively:

$$C = \bar{C}(x,t) + C'(x,y,t)\ ,\ u_x(y) = \tilde{\mathcal{U}} + u'(y)\ ,\ \tilde{\mathcal{U}} = < u_x(y) >\ ,\ \partial_y C'|_{y=0,H} = 0\ , \tag{27}$$

where $\bar{C}(x, t)$ obeys (cf. Eq. (3) with $U_x(y) \to u_x(y)$):

$$\partial_t \bar{C} + \tilde{\mathcal{U}}\partial_x \bar{C} = D_0(1 + k_T^{(a)})\partial_x^2 \bar{C}\ ,\ \text{ where } k_T^{(a)} = -\frac{\partial_x < u'C' >}{D_0 \partial_x^2 \bar{C}}\ . \tag{28}$$

The purpose is to estimate $k_T^{(a)}$. Similar to Eq. (4), it will be obtained with the help of the closure Taylor Ansatz: $D_0\partial_y^2 C' \approx u'(y)\partial_x \bar{C}$, which can be justified by the perturbation analysis assuming that the fastest transport happens in the normal direction. Hence,

$$D_0\partial_y^2 C' \approx u'(y)\partial_x \bar{C}\ ,\ \text{then } C'(x,y,t) = \frac{\gamma(y)}{D_0}\partial_x \bar{C}(x) \text{ and } k_T^{(a)} \approx -\frac{1}{D_0^2} < u'(y)\gamma(y) >\ ,\ \text{with}$$

$$\gamma(y) = \int_0^y [\int_0^y u'(y')\mathrm{d}y']\mathrm{d}y' + C_1 y + C_2\ ,\ < u'(y) > = 0\ . \tag{29}$$

Notice that the integration constants do not impact $k_T^{(a)}$ and they are omitted below. The combination of Eqs. (23) and (24) for $n = 0, 1, \cdots, H-1$ yields:

$$\Delta_y^2 \gamma(n) = u'(n)\ ,\ u'(n) = \mathcal{U}(\delta U^{(a)}(n) - \delta\mathcal{U}^{(a)})\ ,\ \Delta_y^2\gamma = \gamma(n+1) - 2\gamma(n) + \gamma(n-1). \tag{30}$$

After the discrete integration of the last equation, with $\Delta_y^2 \frac{k^{1+n}}{(k-1)^2} = k^n$, the solution reads

$$\gamma(n) = \frac{k^{-n}(Hk(k^{2n} + k^N) - n^2 k^n(-1+k)(-1+k^{1+N}))}{H(-1+k)^2(-1+k^N)}\ ,\ n = 0, 1, \ldots, N = H-1\ . \tag{31}$$

The expression for $k_T^{(a)}$ in Eq. (29) is then rather complicated, and it simplifies for $\Lambda = \frac{1}{4}$:

$$U_x = const\ ,\ \Lambda = \frac{1}{4}\ :\ k_T^{(a)} \approx \frac{(H-1)(H-2)}{H^2}\frac{(1-2t_c^{(a)})^2 Pe^2}{12H^2}\ ,\ k_T^{(a)}|_{H\to\infty} \approx \frac{(1-2t_c^{(a)})^2 Pe^2}{12H^2}\ . \tag{32}$$

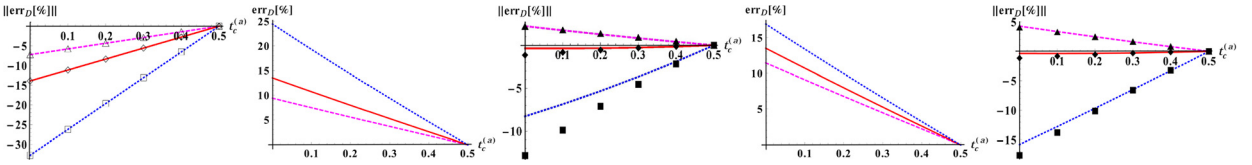

Fig. 12. (Color online.) This figure compares the BB and SL numerical results for $\|\mathrm{err}_D(t_c^{(a)})\|$ with the sum of truncation and boundary-layer dispersions. First diagram: $\|\mathrm{err}_D(t_c^{(a)})\|$ in d2Q9-SNL serves as a truncation error. Second diagram: predicted boundary-layer contribution for BB, $\|\mathrm{err}_D(t_c^{(a)})\| = k_T^{(a)}/(1+k_T)$ with $k_T^{(a)}$ from Eq. (33). The third diagram sums the two first ones and compares results (lines) with the numerical data (symbols) for $\Lambda = \frac{1}{6}$ ("triangles"), $\Lambda = \frac{1}{4}$ ("lozenges"), $\Lambda = \frac{1}{2}$ ("squares"). The first and the two last diagrams display the same procedure for local-specular reflection SL.

This solution is quite interesting. Firstly, as the physical dispersivity coefficient k_T in parabolic profile, $k_T^{(a)}$ scales as Pe^2 and hence $\mathrm{err}_D = k_T^{(a)}$ grows infinitely with Pe^2 in c-field. Secondly, it remains constant when the model parameters are fixed and Pe linearly increases with H. Thirdly, it increases as a square of the diagonal velocity-weight value $t_d^{(a)} = (1-2t_c^{(a)})/4$. The right diagram in Fig. 7 shows that the constructed dispersion matches surprisingly well the numerical data for $\mathrm{err}_D(t_c^{(a)})$ in small box $H = 12$. Further simulations (data are not shown) confirm that $\|\mathrm{err}_D\|$ takes nearly the same values with $H = 24$ and $H = 36$ for the same mean velocity values, such as $\mathcal{U} = \{1/60, 1/30\}$, and the results are found in very good agreement with the predictions when $\Lambda \in [1/400, 9/4]$. The relatively small difference observed can be explained by the associated truncated numerical dispersion, similar to the one existing in parabolic profile and given by Eq. (5). This hypothesis is in line with the fact that the best agreement is observed for $\Lambda = \frac{1}{4}$ and $\Lambda = \frac{1}{6}$ (these two values cancel some of the coefficients in truncation errors), and also, because the difference between the theoretical predictions and numerical results increases with Λ, as the truncation coefficients. Finally, we have carefully checked that the entire numerical value $\|\mathrm{err}_D\|$ presents the sum of three separate contributions, from (i) mass-weight $t_d^{(m)}$, (ii) U_x^2-weight $t_d^{(u)}$ and (iii) velocity weight $t_d^{(a)}$ (see Fig. 7). However, in the presented results, the dispersion due to $t_d^{(a)}$ exceeds the two other effects by several orders of magnitude.

In summary, the Taylor dispersion induced by the variation of the boundary-layer velocity field explains the apparent huge diffusion corrections observed in Figs. 6 and 7. Therefore, in isotropic solute transport by the plug flow, a preference should be given to d2Q5-BB/d2Q9-SNL schemes, which is in agreement with the free-slip boundary conditions offered by the specular-forward reflection in the hydrodynamic modeling.

4.4.2. Poiseuille profile

We suggest now that the apparent dispersivity coefficient $k_T + k_T^{(a)}$ in Figs. 1 and 4 results from the superposition of the two velocity fields: the p-field $U_x(y)$ and the boundary-layer distribution $\mathcal{U}\delta U^{(a)}(n)$ given by Eq. (25), with the mean value $\mathcal{U}\delta\mathcal{U}^{(a)}$ given by Eq. (26):

$$k_T + k_T^{(a)} = -\frac{1}{D_0^2} < (U'(y) + \delta U'(y))(\alpha(y) + \gamma(y)) > ,\ k_T = -\frac{1}{D_0^2} < U'(y)\alpha(y) > ,\ \text{with}$$

$$\alpha(y) = \int_0^y [\int_0^y U'(y)\mathrm{d}y']\mathrm{d}y' ,\ \gamma(y) = \int_0^y [\int_0^y \delta U'(y)\mathrm{d}y']\mathrm{d}y' ,$$

$$U'(y) = U_x(y) - < U_x(y) > ,\ \delta U'(y) = \mathcal{U}(\delta U^{(a)}(y) - < \delta U^{(a)}(y) >) . \tag{33}$$

Here the value of k_T is the same as in Eq. (4), while $k_T^{(a)}$ is due to the boundary-layer velocity gradients and to the superposition of two velocity fields. Discrete integration is applied to obtain $\gamma(n)$ and the averaging is obtained via summation. In order to compare the obtained dispersivity coefficient $k_T^{(a)}$ with the numerical predictions, one needs to know the truncation dispersion of the numerical scheme. Since d2Q9-SNL gives a value of $\mathrm{err}_D(t_c^{(a)})$ close to the truncation predictions (the fourth column in Fig. 4) and exactly equal to the fully periodic solution, we sum $\mathrm{err}_D(t_c^{(a)})$ from d2Q9-SNL (the first diagram in Fig. 12) with $k_T^{(a)}$ from Eq. (33) (the second diagram in Fig. 12) and compare this result (on the third diagram in Fig. 12) with the numerical results (which are taken from the first diagram in the bottom row in Fig. 4). We find again that the agreement is excellent for $\Lambda = \frac{1}{6}$, while the deviation increases with Λ. On the whole, the boundary-layer numerical dispersion captures the main effect of the presented simulations with $\Lambda \geq \frac{1}{12}$, where the truncation and boundary-layer dispersion corrections have opposite signs and almost compensate each other. When $\Lambda < \frac{1}{12}$, the situation should reverse for $\|\mathrm{err}_D\|$, because both the boundary-layer dispersion and the difference with d2Q5 in Eq. (5) become positive. Increasing the velocity by a factor of 2 (as in Fig. 1) yields very similar results for err_D because as Pe increases, the truncation and boundary-layer dispersion corrections (in the nominator), and the k_T (in the denominator), both scale as Pe^2. Finally, the next two diagrams in Fig. 12 show even a better agreement employing a similar procedure for the d2Q9-SL, where $k_T^{(a)}$ was built with Eq. (33) by using the approximate solution for $\delta U'(y)$ from Fig. 11.

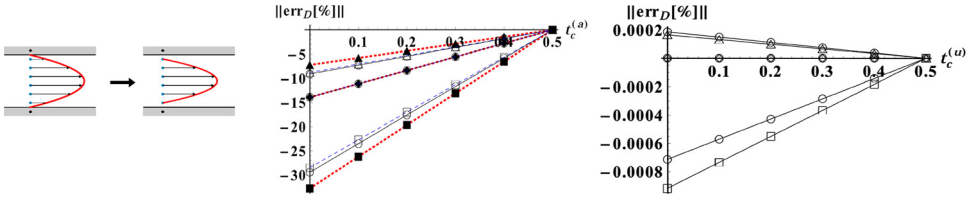

Fig. 13. (Color online.) The numerical results for $\|\mathrm{err}_D\|(t_c^{(a)})$ (middle diagram) and $\|\mathrm{err}_D\|(t_c^{(u)})$ (right diagram) are obtained with the d2Q9-BB ("empty" symbols), d2Q9-SL ("empty" circles) and d2Q9-SNL (dark symbols) in p-field when the zero velocity is shifted toward the boundary grid node (left diagram). The three reflections coincide for $\Lambda = \frac{1}{4}$.

In summary, the positive boundary-layer dispersion explains the apparent improvement of $\|\mathrm{err}_D\|$ in Fig. 4 with the BB and SL over the SNL. However, this implies an alteration of the advection flow.

5. Reduction of boundary layers

We consider two possibilities for the reduction or the elimination of the non-equilibrium boundary layers applying the bounce-back and local specular reflection. The purpose is twofold: first, we aim at verifying our analysis from another perspective; second, we attempt to produce some simple practical strategies.

5.1. Grid-node location of the zero-velocity value in the parabolic profile

The idea is that the boundary-layer profile (25) would vanish if the zero-velocity value were located in the grid node itself: $U_x(\mathbf{r}_b) = 0$ (see the left-hand-side diagram in Fig. 13). Indeed, by prescribing such a profile for $U_x(y)$ in $e_{\bar{q}}$, we observe that $\|\mathrm{err}_U(t_c^{(a)})\|$, presented in Fig. 11, completely vanishes with BB and SL. Fig. 13 shows that their solutions for $\|\mathrm{err}_D(t_c^{(a)})\|$ very closely approach each other and d2Q9-SNL; a still existing small difference might be explained by the higher-order truncation dispersion. Furthermore, the three solutions coincide for $\Lambda = \frac{1}{4}$. It is in line with $\|\mathrm{err}_D(t_c^{(u)})\|$, which completely vanishes when $\Lambda = \frac{1}{4}$, and otherwise is reduced in amplitude (cf. the right-hand-side diagram in Fig. 13 and the diagram in the middle of Fig. 11). However, a systematic location of the no-slip velocity in the grid nodes cannot be recommended. Firstly, it is not handled by the bounce-back in flow modeling where the leading-order approximate is the halfway location. Second, even if the zero distance is formally accessible with the alternative hydrodynamic boundary conditions, their solutions may become non-unique in corners (see [13]). Thirdly, this technique only applies for rectangular boundaries. Therefore, this first example is mainly of methodological interest.

5.2. Elimination of boundary layers with small boundary values of Λ

In plug flow the amplitude of the mean induced velocity in Eq. (24) scales nearly as $\sqrt{\Lambda}$. This is also a leading asymptotic Λ-scaling for parabolic flow, according to Eq. (26)(a). In agreement with the presented results, the uniform small-valued Λ reduces the effect of the boundary layers. However, the small-valued Λ may cause the instability of the scheme when the imposed velocity approaches its stability limit $\mathcal{U} = \mathcal{U}^{\max}$, especially in the high-Pe range when $c_e \to 0$ or $\Lambda^- \to 0$ [28,26]. For instance, in the numerical example considered here with $\mathcal{U} = \mathcal{U}^{\max}/2$, the BGK model with $\Lambda = (\Lambda^-)^2 = 1/400$ is stable in both c-field and p-field only when $t_c^{(a)} \in [0.4, 0.5]$ and $t_c^{(m)} \in [0.3, 0.5]$. Therefore, only in the low-Pe range, the use of small values, as $\Lambda = \frac{1}{12}$, is suitable.

The straightforward idea is to drop Λ to a very small value Λ_b, but only in the boundary nodes, because the boundary layers are excited there. Fig. 14 displays such results for the bounce-back in c-field, retaining $\Lambda \in \{\frac{1}{6}, \frac{1}{4}, \frac{1}{2}\}$ everywhere, except in the grid-boundary nodes where $\Lambda_b = (\Lambda^-)^2 = 1/400$. Firstly, $\|\mathrm{err}_U\|$ and $\|\mathrm{err}_D\|$ both diminish drastically and the results for the three values Λ remain stable and almost coincide. Secondly, the effects of the boundary layers are larger than those predicted for this small but uniform Λ value, where simulations are however unstable. Thirdly, the profiles are clearly improved, but they indicate that still a smaller value Λ_b is needed to capture the analytical solution. The results from similar simulations conducted in p-field are presented in Fig. 15. The obtained small boundary-layer velocity amplitude (second diagram) reduces the associated dispersion error (third diagram) and the concentration profiles (fourth diagram), then practically coincide with the d2Q9-SNL result. These simulations were stable with respect to the individual or joined-weight variations, and more stable than in c-field. An interesting observation in Fig. 15 is that $\|\mathrm{err}_U\|$ becomes positive. Our further investigations have shown that by extending interface flow analysis [29] to boundary layers, it becomes possible to analytically predict H-dependent solution for boundary value Λ_b (versus bulk value Λ_v) which *completely eliminates* the bounce-back velocity error in Poiseuille profile. However, a similar solution in plug flow makes Λ_b negative. Thereby, the altering of the diffusion coefficient due to the diagonal mass weight also cannot be *vanished* with the help of Λ_b alone, but a small-valued Λ_b *reduces* all spurious effects noticeably.

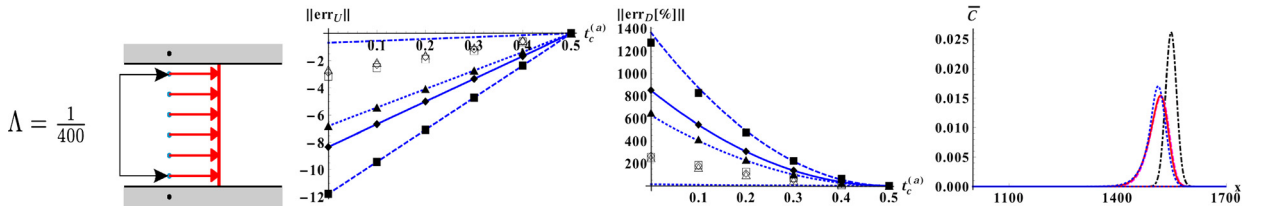

Fig. 14. (Color online.) The d2Q9-BB model when Λ is reduced to $1/400$ uniquely in boundary nodes $y = \{\frac{1}{2}, H - \frac{1}{2}\}$. This numerical solution is plotted with "empty symbols", the previous solution for uniform Λ with "dark symbols": $\Lambda = \frac{1}{6}$ ("triangles"), $\Lambda = \frac{1}{4}$ ("lozenges"), $\Lambda = \frac{1}{2}$ ("squares"). The prediction for uniform value $\Lambda = 1/400$ is plotted by a dash-dotted line (without symbols).

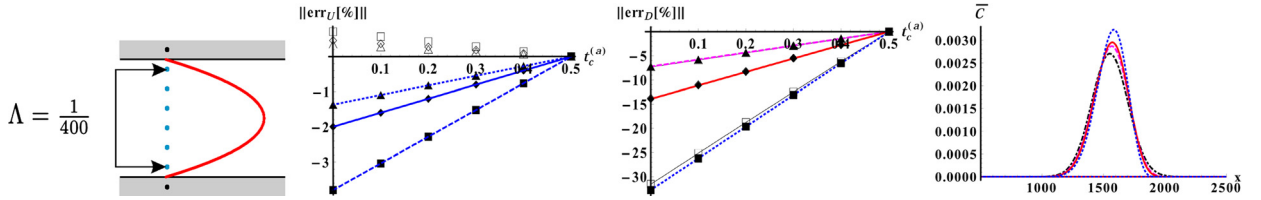

Fig. 15. (Color online.) Similarly as in Fig. 14 but in the parabolic profile, with $\Lambda_b = 1/400$ in grid boundary nodes. The dispersion errors and concentration profiles almost coincide for d2Q9-BB (plotted here) and d2Q9-SNL (see Figs. 4c and 5c).

6. Concluding remarks

The effect of the local mass-conserving boundary schemes for the Neumann boundary condition in the advection–diffusion d2Q9 scheme is investigated. Steady-state recurrence equations satisfying the LB equations and the bounce-back boundary rule are solved in a closed analytical form with respect to the exponentially decaying accommodation non-equilibrium boundary layers. We call them "spurious" because they are unintended and caused by the incompatibility of the zero tangential boundary flux with the ADE bulk solution. The novel point is that these accommodation layers modify the macroscopic second-order equations predicted by the Chapman–Enskog and asymptotic analysis. Their main three effects are: (i) slowing-down advection front proportionally to the diagonal velocity weight $t_d^{(a)}$, (ii) decrease of the diffusion coefficient proportionally to the diagonal mass-weight $t_d^{(m)}$, and (iii) creation of the numerical longitudinal Taylor dispersion, because of the transverse velocity gradient. Although derived from the steady-state recurrence equations, the averaged diffusion and velocity corrections are exact on the measured moments due to the invariance with respect to the moving frame. The two corrections, diffusion and advection, only linearly decrease with the space resolution, similarly to the bounce-back flow effect on the inclined [16] or curved [24] walls. A huge velocity and dispersion effect takes place in the plug flow because of the absence of the mechanical dispersion. In parabolic profile, the averaged velocity correction scales with the prescribed boundary-node velocity value, the associated numerical dispersion scales as Pe^2, a sum of the mechanical, truncation and boundary-layer dispersion explains the measured apparent dispersivity coefficient.

A fascinating signature of the boundary layers is that their primary effects grow as $\sqrt{\Lambda}$ while the coefficients of the bulk truncation errors scale polynomially with Λ [20,12]. It is often believed that Λ only impacts the high-order corrections, e.g., [18]; however, it is not so in the presence of boundaries [23,17,13,14,24]. Employing an inadequate boundary rule in the ADE, Λ impacts the advection–diffusion flux and therefore, the first and the second distribution moments. In order to improve the entire computations, the idea we suggest is to use a small value Λ_b at boundary points, while using another suitable (e.g., optimal) value Λ_v in the bulk. Although a small-valued uniform Λ drops the stable velocity amplitude [28,12, 26], this isn't a drawback near the wall where velocities are low. During revision of this work, exact solution $\Lambda_b(\Lambda_v)$, where the prescribed advection velocity is preserved, has been derived in straight Poiseuille profile. Furthermore, all presented solutions have been extended for the benchmark modeling of the Taylor dispersion in a circular pipe. In particular, it has been discovered that the d3Q7 − BB scheme does not create any boundary layers. Therefore, the diagonal links do not necessarily improve for the boundary accuracy on the complex shapes—contrary to the common expectations. The specific solution $\Lambda_b(\Lambda_v)$ effectively reduces the velocity-weight boundary-layer effects in d3Q15 − BB scheme for circular pipe. All these results will be reported elsewhere. Altogether, this encourages our idea that, by applying local mass-conserving boundary schemes, the reduction of their spurious effects can be achieved on the arbitrarily-shaped boundaries with the help of the properly distributed Λ.

Acknowledgements

The authors thank Alexander Vikhansky for help and ANR for funding the project LaboCothep ANR-12-MONU0011.

References

[1] C. Cercignani, in: The Boltzmann Equation and Its Applications, Springer, Berlin, 1988, pp. 252–260.
[2] F. Verhaeghe, L.-S. Luo, B. Blainpain, Lattice Boltzmann modeling of microchannel flow in slip flow regime, J. Comput. Phys. 228 (2009) 147–157.
[3] T. Reis, P.J. Dellar, Lattice Boltzmann simulations of pressure-driven flows in microchannels using Navier–Maxwell slip boundary conditions, Phys. Fluids 24 (2012) 112001.
[4] C. Baudet, J.-P. Hulin, D. d'Humières, P. Lallemand, Lattice-gas automata: a model for the simulation of dispersion phenomena, Phys. Fluids 1 (1989) 507–512.
[5] A. Cali, S. Succi, A. Cancelliere, R. Benzi, M. Gramignani, Diffusion and hydrodynamic dispersion with the lattice Boltzmann method, Phys. Rev. A 45 (8) (1992).
[6] E.G. Flekkoy, U. Oxaal, J. Feder, T. Jossang, Hydrodynamic dispersion at stagnation points: simulations and experiments, Phys. Rev. Lett. 77 (1995) 4952–4962.
[7] G.I. Taylor, Dispersion of soluble matter in solvent flowing slowly through a tube, Proc. R. Soc. Lond. A 219 (1953) 186–203.
[8] R. Aris, On the dispersion of a solute in a fluid flowing through a tube, Proc. R. Soc. Lond. 235 (1956) 67–77.
[9] G. Drazer, J. Koplik, Tracer dispersion in two dimensional rough fractures, Phys. Rev. E 63 (2001) 056104.
[10] I. Ginzburg, Generic boundary conditions for Lattice Boltzmann models and their application to advection and anisotropic–dispersion equations, Adv. Water Resour. 28 (2005) 1196–1216.
[11] I. Ginzburg, D. d'Humières, A. Kuzmin, Optimal stability of advection–diffusion lattice Boltzmann models with two relaxation times for positive/negative equilibrium, J. Stat. Phys. 139 (6) (2010) 1090–1143.
[12] I. Ginzburg, Truncation errors, exact and heuristic stability analysis of two-relaxation-time lattice Boltzmann schemes for anisotropic advection–diffusion equation, Commun. Comput. Phys. 11 (5) (2012) 1439–1502.
[13] I. Ginzburg, F. Verhaeghe, D. d'Humières, Two-relaxation-time lattice Boltzmann scheme: about parametrization, velocity, pressure and mixed boundary conditions, Commun. Comput. Phys. 3 (2008) 427–478.
[14] I. Ginzburg, F. Verhaeghe, D. d'Humières, Study of simple hydrodynamic solutions with the two-relaxation-time lattice Boltzmann scheme, Commun. Comput. Phys. 3 (2008) 519–581.
[15] Y. Qian, D. d'Humières, P. Lallemand, Lattice BGK models for Navier–Stokes equation, Europhys. Lett. 17 (1992) 479–484.
[16] I. Ginzbourg, D. d'Humières, Local second-order boundary method for lattice Boltzmann models, J. Stat. Phys. 84 (1996) 927–971.
[17] I. Ginzburg, D. d'Humières, Multi-reflection boundary conditions for lattice Boltzmann models, Phys. Rev. E 68 (2003) 066614.
[18] L. Li, R. Mei, J.F. Klausner, Boundary conditions for thermal lattice Boltzmann equation method, J. Comput. Phys. 237 (2013) 366–395.
[19] T. Gebäck, A. Heintz, A lattice Boltzmann method for the advection–diffusion equation with Neumann boundary conditions, Commun. Comput. Phys. 15 (2) (2014) 487–505.
[20] D. d'Humières, I. Ginzburg, Viscosity independent numerical errors for lattice Boltzmann models: from recurrence equations to "magic" collision numbers, Comput. Math. Appl. 58 (5) (2009) 823–840.
[21] R. Cornubert, D. d'Humières, D. Levermore, A Knudsen layer theory, Physica D 47 (1991) 241–259.
[22] I. Ginzbourg, Les problèmes des conditions aux limites dans les méthodes de gaz sur réseaux à plusieurs phases, PhD thesis, University of Paris-6, 1994.
[23] I. Ginzbourg, P.M. Adler, Boundary flow condition analysis for the three-dimensional lattice Boltzmann model, J. Phys. II 4 (1994) 191–214.
[24] S. Khirevich, I. Ginzburg, U. Tallarek, Coarse- and fine-grid numerical behavior of MRT/TRT lattice Boltzmann schemes in regular and random sphere packings, J. Comput. Phys. 281 (2015) 708–742.
[25] X. Yin, G. Le, J. Zhang, Mass and momentum transfer across solid-fluid boundaries in the lattice-Boltzmann method, Phys. Rev. E 86 (2012) 026701.
[26] L. Roux, I. Ginzburg, Truncation effect on Taylor–Aris dispersion in two-relaxation-times Lattice Boltzmann scheme: accuracy towards stability, J. Comput. Phys. 299 (2015) 974–1003.
[27] I. Ginzburg, Multiple anisotropic collisions for advection–diffusion lattice Boltzmann schemes, Adv. Water Resour. 51 (2013) 381–404.
[28] A. Kuzmin, I. Ginzburg, A.A. Mohamad, A role of the kinetic parameter on the stability of two-relaxation-time advection–diffusion lattice Boltzmann scheme, Comput. Math. Appl. 61 (12) (2011) 3417–3442.
[29] I. Ginzburg, G. Silva, L. Talon, Analysis and improvement of Brinkman lattice Boltzmann schemes: bulk, boundary, interface. Similarity and distinctness with finite elements in heterogeneous porous media, Phys. Rev. E 91 (2) (2015) 023307.